



A Spatially Explicit, Multi-nutrient, Multi-species Plankton Model for Shallow Bay Systems

Sierra E. Cagle¹ · Daniel L. Roelke¹ · Joydeb Bhattacharyya²

Received: 14 November 2022 / Revised: 21 April 2023 / Accepted: 26 April 2023 / Published online: 1 June 2023
© The Author(s), under exclusive licence to Coastal and Estuarine Research Federation 2023

Abstract

Worldwide, shallow bay systems are impacted by altered freshwater inflows and nutrient loading. To facilitate predictions of phytoplankton abundance and dissolved oxygen responses to altered inflows, we develop a spatially explicit, multi-nutrient, multi-species model (MUMPS) for shallow bay systems, then use data from the San Antonio Bay System (SABS), USA, for training. Through sensitivity and simulation analyses, we found that the phytoplankton biomass of SABS, under historically averaged conditions, is likely controlled by a combination of cell loss through hydraulic displacement and light limitation. However, modest reductions in river discharge diminished hydraulic displacement of cells, allowing for increased phytoplankton biomass. It also led to increases in the yearly dissolved oxygen minimum, which was associated with the greater phytoplankton biomass. Additionally, decreasing river discharge altered how river nutrient concentrations influenced phytoplankton biomass in SABS, resulting in a state where nutrient reductions became more effective with decreasing discharge. Importantly, reduced inflows led to a regional shift in phytoplankton biomass from the lower bay towards the middle bay. Regional shifts in phytoplankton biomass in SABS arising from altered river discharges, such as suggested by our model, may be impactful to sessile organisms (e.g., oysters), organisms of limited dispersal (e.g., juvenile blue crabs), and the organisms that feed on these (e.g., endangered whooping cranes for the case of blue crabs).

Keywords Bio-physical model · Inflows · Nutrient loading · Phytoplankton biomass · Dissolved oxygen

Introduction

Estuaries are coastal aquatic systems that are characterized by a transition from fresh to salt waters. Geological morphology, tidal exchanges, and freshwater inflows are important in defining these systems and largely determine salinity variation both spatially and temporally (Hansen and Rattray 1966; Ketchum 1983). The dynamic nature of many estuarine systems requires that organisms found there be adapted to deal with such conditions (Costanza 1997; Day et al. 2013). However, it is also this dynamic nature which creates an environment suited to act as a nursery for

the young of marine and estuarine organisms (Gillanders et al. 2003; Day et al. 2013), many of which are important to commercial fisheries. Beyond their value to fisheries, estuaries are recognized for their recreational, ecosystem service, and intrinsic biological values (Pendelton 2010; Barbier et al. 2011).

These vital ecosystems are under threat from various directions including rapid population growth, uncontrolled development, and climate change, factors which have led to a number of issues such as increased pollution inputs, loss or degradation of habitat, and variation to freshwater inflows (Kennish 2002). Changes in the natural magnitude and frequency of freshwater inflows to estuarine systems are especially concerning given the critical role they play in determining their form and function (Ketchum 1951, 1954; Hildebrand and Gunter 1953; Odum et al. 1995; Roelke and Pierce 2011; Nordhaus et al. 2018). Freshwater inflows influence both estuarine biogeochemical processes (Webster and Harris 2004; Bruesewitz et al. 2013; Islam et al. 2014; Hitchcock and Mitrovic 2015; Hitchcock et al. 2016) and biota (Tolan 2008; Wozniak et al. 2012; Roelke et al. 2013,

Communicated by James L. Pinckney

✉ Sierra E. Cagle
SEC1414@tamu.edu

¹ Department of Marine Biology, Texas A&M University at Galveston, 200 Seawolf Parkway, Galveston, TX 77554, USA

² Department of Mathematics, Karimpur Pannadevi College, Nadia, West Bengal 741152, India

2017; Palmer and Montagna 2015; Lehrter and Le 2017) in a number of ways. Concerning phytoplankton, which play a major role in determining water quality, freshwater inflows influence rates of photosynthesis and community respiration (Russell et al. 2006; Roelke et al. 2013, 2017), as well as assemblage composition (Roelke et al. 1997, 2013, 2017; Robson and Hamilton 2003; Spatharis et al. 2007a, b; Dorado et al. 2015; Pinckney et al. 2017).

In Texas estuaries, located along the Western Gulf of Mexico where this work is focused, empirical studies have indicated the importance of freshwater inflows for a myriad of environmental processes. These include primary productivity and community respiration (Russell et al. 2006; Roelke et al. 2013, 2017), phytoplankton assemblage composition (Örnólfssdóttir et al. 2004; Roelke et al. 1997, 2013, 2017; Dorado et al. 2015), wetland plant health (Wozniak et al. 2012), invertebrate and vertebrate population dynamics (Tolan 2008; Palmer and Montagna 2015), and overall food web health (Montagna et al. 2011).

As in other regions of the world, Texas estuaries face potential alteration of freshwater inflows. In the present study, we focus on the influence of inflows on the San Antonio Bay System (SABS), one of Texas' 7 major estuaries. Here, changing land usage in the upstream water sheds (San Antonio River Basin and Guadalupe River Basin) has the potential to alter freshwater inflow patterns and their associated nutrient loads. The effects of water shed changes on discharges to an estuary are complex, especially when considering the coupled effects of climate change, but likely influence nutrient loading as well as the magnitude and timing of freshwater arrivals to the SABS. Previous work has demonstrated that increased urbanization in the San Antonio River Basin will likely cause increased variability in streamflow (Shao et al. 2020). And, the Texas Water Development Board (South Central Regional Water Planning Group 2020) has predicted the need for water in the region (which encompasses portions of both river basins) to increase by nearly 300,000 acft/yr (~25% increase) from year 2020 to 2070, while the supply is expected to increase by only about a 12,000 acft/yr over the same time period. This increase is largely associated with heavy population growth and development of municipalities in the region. Further, nutrient loads in both water sheds have been shown to correlate with developed land use (Arismendez et al. 2009), suggesting that SABS nutrient loading is likely to continue increasing along with projected development. Such findings suggest that SABS is likely to see changes in nutrient loading and freshwater inflows in the future, if not already.

Previous work investigating the influence of inflow reductions on various aspects of bay functioning has suggested various outcomes, including from little to no change in fisheries and the endangered whooping crane

population (Slack et al. 2009) to regional shifts or reductions in productivity and possible negative food chain effects (Paudel and Montagna 2014; Roelke et al. 2017). Such alterations to patterns in phytoplankton biomass and productivity have the potential to influence the food web (Day et al. 2013), especially less mobile and sessile organisms like oysters (Laing and Chang 1998), but also impact physico-chemical aspects of the system like water column dissolved oxygen (Odum 1956).

To better understand the relationship between inflows, nutrient loading, dissolved oxygen, and phytoplankton biomass in different regions of the SABS, a novel numerical model was developed. Determination of model structure was guided by statistical analyses of historical data from the SABS (Roelke and Bhattacharyya 2017), and generalized ecological and physico-chemical principals were incorporated, thereby creating a computational tool with potential for transport across estuarine ecosystems. A model training process was conducted using high-dimensional, short-period (2 years) data (Gable 2010; Roelke et al. 2017) that covered a gradient of wet to dry hydrologic conditions in the SABS. Subsequent simulation analyses allowed for the exploration of various inflow and nutrient loading regimes on phytoplankton biomass and dissolved oxygen levels in the upper, middle, and lower regions of the SABS.

Methods

Study Area

The San Antonio Bay System (SABS) is comprised of multiple bays encompassing about 530 km², with San Antonio Bay being the dominant feature, having an area of 288 km². Smaller bays comprising SABS include Hynes Bay (area 28 km²) and Guadalupe Bay (area 12.5 km²). Freshwater inflow enters the SABS primarily from the Guadalupe River, which is formed from the confluence of the Guadalupe and San Antonio Rivers upstream of the discharge point. A barrier island, Matagorda Island, separates the SABS from the Gulf of Mexico, restricting tidal exchange, resulting in little direct water exchange between the SABS and ocean waters. Water exchange with the Gulf of Mexico takes place through distant passes, Pass Cavallo, at the northeast end of Matagorda Island, and Cedar Bayou, an intermittently open-closed channel to the southwest. Using the long-period data provided by TCEQ's SWQMIS (described below), it was determined that the 27-year average salinity in upper SABS was 5.4 psu, whereas the 27-year average salinity in middle SABS and in lower SABS was 12.9 psu and 16.9 psu, respectively. The average water temperature in SABS ranges from 13.4 °C in the winter to 30.4 °C in the summer.

Historical Data

Data collected from the Roelke Lab appears in Roelke et al. (2017) and Gable (2010) and was used for model training. These data sets are comprised of monthly samplings carried out over a period of 30 months at six fixed stations (Fig. 1a) from March 2004 to August 2006 where a suite of physical, chemical, and biological parameters was sampled. This data also includes daily freshwater inflow from the San Antonio and Guadalupe Rivers, compiled from gauged data (USGS gauges 08188500 and 08176500, respectively) for the entire 30-month period of study (Fig. 1b). Parameters from the full data set that were used in this work include NH_4 , NO_x , soluble reactive phosphorous (SRP), chlorophyll *a* (Chl*a*), dissolved

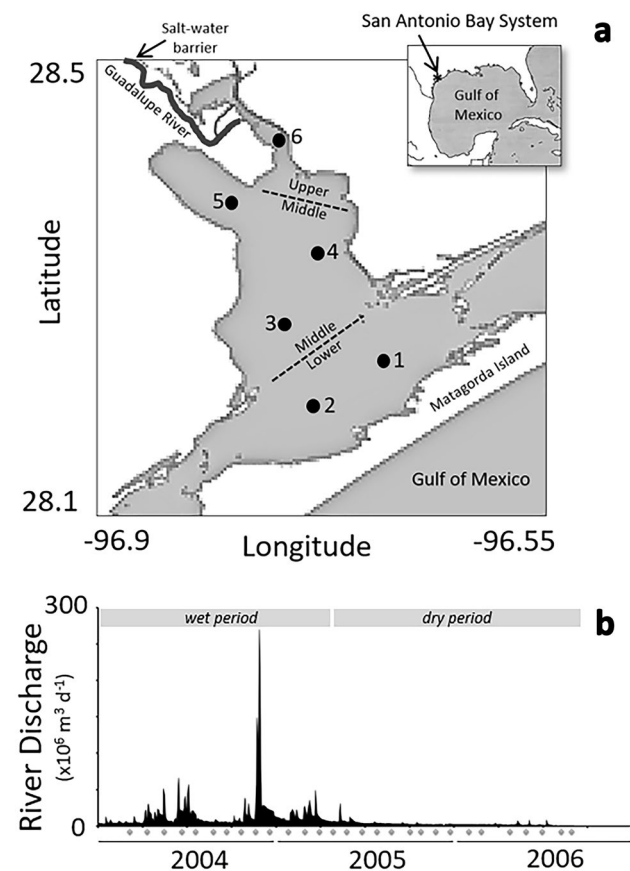


Fig. 1 Historical data for the San Antonio Bay System (SABS) was used for model training. **a** The SABS sampling stations where data was collected by the Roelke laboratory at Texas A&M University Galveston. **b** River discharges entering the SABS with data from US geologic service monitoring gauges (Roelke laboratory sampling dates are shown by blue diamond). The SABS samplings spanned both relatively wet and dry periods

oxygen (DO), and combined freshwater inflows. Inflows, as well as daily nutrient and Chl*a* loadings to the upper region of the SABS were determined using the gauged flow data along with nutrient (μM) and Chl*a* concentrations ($\mu\text{g L}^{-1}$) from a sampling station in the Guadalupe River. The river sampling station was located downstream of the confluence of the San Antonio and Guadalupe Rivers, and sampling at this site took place during the Roelke et al. (2017) study, though the data was not used in those analyses. Two additional sampling sites from adjacent systems were used to generate data for end-member loadings. These included a site in Mesquite Bay and another site in Espiritu Bay, to the west and east of the SABS, respectively. For the lower region of the SABS, associated end-member loading of nutrients and Chl*a* was determined with modeled water exchanges (TxBLEND) along with nutrient (μM) and Chl*a* concentrations ($\mu\text{g L}^{-1}$) from the adjacent bay systems. For our sensitivity and simulation analyses, these water exchanges were standardized, as will be described below.

Longer period data were used to calculate 27-year averages of seasonal inflows and river nutrient concentrations. These were used during the sensitivity and simulation analyses. This data was provided by the Texas Commission for Environmental Quality's (TCEQ) Surface Water Quality Monitoring Information System (SWQMIS) and USGS flow gauges mentioned previously.

Model Development

Phytoplankton Growth

Phytoplankton taxonomic groups observed in SABS samples (Roelke, unpublished) included species with widely varying salinity preferences; therefore, phytoplankton functional groups were incorporated into the model, instead of taxonomic groups. Freshwater, estuarine, and marine phytoplankton functional groups, defined by their salinity tolerances, comprised the model's biological reaction scheme. For these populations, the maximum growth rate (r) was proportionately attenuated by temperature and then by salinity as defined by a population's tolerance range. The temperature- and salinity-attenuated r was then used to determine the realized growth rate (μ) as a function of nutrient concentrations and light availability.

Attenuation of the maximum growth rate by temperature is a piecewise linear approximation of the essentially nonlinear response of growth to temperature (T °C, Eppley 1972) with a Q10 of $q = 3$, based on model training.

$$T(t) \text{ att.} r = \begin{cases} \frac{r}{q^2} \left(1 + \frac{T(t)}{10}\right) \frac{T(t)}{\max(T(t))}, & \text{if } T(t) \leq 10 \\ \frac{r}{q} \left(1 + \frac{T(t)-10}{10}\right) \frac{T(t)}{\max(T(t))}, & \text{if } 10 \leq T(t) \leq 20 \\ r \left(1 + \frac{T(t)-20}{10}\right) \frac{T(t)}{\max(T(t))}, & \text{if } 20 \leq T(t) \leq 30 \\ \frac{2rT(t)}{\max(T(t))}, & \text{if } T(t) \geq 30 \end{cases} \quad (1)$$

Given $r=2$, following these equations over the range of temperatures observed in the SABS, temperature-attenuated growth rates range from 0.15 to 2.0 d^{-1} .

For the freshwater phytoplankton species, it is assumed that the growth rate decreases with the increase of salinity (s). Therefore, the relationship between freshwater phytoplankton growth rate and salinity takes the form

$$s_i(t) \text{ att.} r = \begin{cases} r \left(\frac{s_i(t) - s_{\max}^F}{s_{\max}^F} \right)^2, & 0 \leq s_i(t) \leq s_{\max}^F \\ 0, & s_i(t) > s_{\max}^F \end{cases} \quad (2)$$

where $s_i(t)$ is the salinity of region i at time t , and s_{\max}^F is the maximum sustainable salinity threshold for the growth of freshwater phytoplankton species. For estuarine phytoplankton species, the salinity-attenuated growth rate is assumed to be a unimodal function of salinity, which starts decreasing when the salinity becomes higher than some optimal salinity threshold. Therefore, the relationship between estuarine phytoplankton growth rate and salinity takes the form

$$s_i(t) \text{ att.} r = \begin{cases} r \sqrt{\frac{s_i(t) - s_{\min}^E}{s_{\text{opt}}^E - s_{\min}^E}}, & s_{\min}^E \leq s_i(t) \leq s_{\text{opt}}^E \\ r \sqrt{\frac{s_{\max}^E - s_i(t)}{s_{\max}^E - s_{\text{opt}}^E}}, & s_{\text{opt}}^E \leq s_i(t) \leq s_{\max}^E \\ 0, & 0 < s_i(t) \leq s_{\min}^E \text{ or } s_i(t) > s_{\max}^E \end{cases} \quad (3)$$

where s_{\max}^E is the maximum sustainable salinity threshold for the growth of estuarine phytoplankton species, s_{\min}^E is the lower threshold, and s_{opt}^E is the salinity level at which maximum growth occurs. Since marine phytoplankton species grow at a relatively higher salinity level, it was assumed that the salinity-attenuated growth rate of marine phytoplankton species would increase with salinity, until the salinity level reached some maximum sustainable salinity threshold. Therefore, the relationship between marine phytoplankton growth rate and salinity takes the form

$$s_i(t) \text{ att.} r = \begin{cases} r \sqrt{\frac{s_i(t) - s_{\min}^M}{s_{\max}^M - s_{\min}^M}}, & s_{\min}^M \leq s_i(t) \leq s_{\max}^M \\ 0, & 0 < s_i(t) < s_{\min}^M \text{ or } s_i(t) > s_{\max}^M \end{cases} \quad (4)$$

where s_{\max}^M is the maximum sustainable salinity threshold for the growth of marine phytoplankton species, and s_{\min}^M is the salinity level below which growth does not occur.

Finally, the minimum of the temperature- and salinity-attenuated r for each phytoplankton population (k , differentiated based on salinity tolerances) in each region (i) was selected and used to calculate further limitations on growth due to nutrients and light conditions:

$$\mu_{i,k_Ts}(t) = \min(T(t) \text{ att.} r, s_i(t) \text{ att.} r) \quad (5)$$

Phytoplankton nutrient-limited growth rates for nitrogen and phosphorous were a function of ambient nutrient concentrations following the Monod equation, with Liebig’s law of the minimum applied. Regarding nitrogen (NH_4 and NO_X), the N-based growth rate for each phytoplankton population (k) in each region (i) at time t , is given by

$$\mu_{i,k_N}(t) = \mu_{i,k_Ts}(t) \left(\frac{\gamma NO_X + (1 - \gamma) NH_4}{K_N + \gamma NO_X + (1 - \gamma) NH_4} \right), \quad (6)$$

where K_N was the half-saturation coefficient growing on nitrogen and γ was the NO_X versus NH_4 preference parameter ($0 \leq \gamma \leq 1$), and all other parameters are the same as previously defined. Regarding phosphorous (SRP), the P-based growth rate for each phytoplankton population (k) in each region (i) at time t , is given by

$$\mu_{i,k_P}(t) = \mu_{i,k_Ts}(t) \left(\frac{SRP}{K_P + SRP} \right), \quad (7)$$

where K_P was the half-saturation coefficient growing on phosphorous.

The phytoplankton light-limited growth rate is a saturating function, given by

$$\mu_{i,k_L}(t) = \mu_{i,k_Ts}(t) \left(\frac{I_i(z)}{a + I_i(z)} \right), \quad (8)$$

where $I(z)$ was the hourly average irradiance at depth z ; z was the average depth of a given SABS model region; $a = (\mu_{\max} \times 0.203 \times 10^{20}) \text{ quanta-cm}^{-2}\text{s}^{-1}$, converted from Huisman (1999); and other parameters are the same as previously defined. Irradiance at mid-depth is taken as representative of the whole water column for this shallow, well-mixed system, where the mid-depth for the upper SABS is 0.5 m, and the mid-depths for the middle and lower SABS were both 1 m. Here, $I(z)$ is determined as in Roelke (2000) and Cagle and Roelke (2021), following Lambert–Beer’s law, and where irradiance integrated over PAR and incident upon the water surface (I_o) is a function of time of year and latitude. Surface irradiance is calculated based on the work of Brock (1981). Light attenuation is a function of Chl a and background turbidity in a given SABS region (i) and was taken as

$$I_i(z) = I_o(H)e^{-(K_a A_{k,i}(t) Cc + K_r)z}, \tag{9}$$

where $I_o(H)$ was the hourly average surface irradiance, K_a was the light attenuation coefficient (based on Chla ($\text{dcm}^2/\mu\text{g-Chla}$; Huisman 1999; Olivieri and Chavez 2000), $A_{k,i}(t)$ was the k^{th} phytoplankton population in SABS region i at any instant t , K_r was the light attenuation coefficient of pure water and tripton (dcm^{-1}), and Cc is chlorophyll a per phytoplankton cell ($\mu\text{g-Chla}/10^6$ cells). To obtain Cc , we assume an average phytoplankton volume (V) of $\frac{64\pi}{3} (\mu\text{m}^3)$ and calculate the carbon content per cell according to Mullin et al. (1966) as $\frac{V^{0.76}}{10^{0.29}} (\mu\text{g-C } 10^{-6} \text{ cells})$. Finally, taking $C : \text{Chla}$ of 83.14 (Cloern et al. 1995), we calculate Cc as $\frac{V^{0.76}}{83.14 \times 10^{0.29}} (\mu\text{g-Chla}/10^6 \text{ cells})$.

The realized growth rates for the phytoplankton populations at time t in a given SABS region were determined using Liebig’s law of the minimum, given by

$$\mu_{i,k}(t) = \min(\mu_{i,k_N}(t), \mu_{i,k_P}(t), \mu_{i,k_L}(t)). \tag{10}$$

Salinity-Dependent Grazing Rate

We introduced the effect of grazing in the system as a function of salinity (s), rather than incorporating a grazer state variable. The Roelke Lab data used for model training contains zooplankton biovolume measurements (copepods, cladocera, rotifers, and protists; Roelke, unpublished), which show the highest biomass of zooplankton occurring at intermediate salinities and lower biomasses at low and high salinity. Here, it is assumed that grazing rates on phytoplankton are greater when zooplankton populations are higher. Because we are not explicitly modeling zooplankton populations, we made the grazing loss a function of available prey and regional salinity, as has been done in previous modeling in other systems (Mandall et al. 2012; Roy et al. 2016). The specific grazing rate in a given region, $g_i(s)$, was taken as

$$g_i = \begin{cases} g_{\max} \sqrt{\frac{s_i(t) - s_{\min}^g}{s_{\text{opt}}^g - s_{\min}^g}}, & \text{if } s_{\min}^g < s_i(t) < s_{\text{opt}}^g \\ g_{\max} \sqrt{\frac{s_{\max}^g(t) - s_i(t)}{s_{\max}^g - s_{\text{opt}}^g}}, & \text{if } s_{\text{opt}}^g < s_i(t) < s_{\max}^g \end{cases} \tag{11}$$

where the minimum sustainable salinity for grazing is s_{\min}^g , the maximum sustainable salinity for grazing is s_{\max}^g , and the optimum salinity for grazing is s_{opt}^g . The specific grazing rate $g_i(s)$ approaches its maximum g_{\max} when $s(t) = s_{\text{opt}}^g$.

Dissolved Oxygen and Respiration Rate

Dissolved oxygen was influenced, in part, by the biological reaction scheme in that oxygen concentrations were a function of algal respiration and Chla concentration. The oxygen

production rate ($\text{mg-O}_2 \text{ L}^{-1} \text{ day}^{-1}$) by the k^{th} phytoplankton species $A_{i,k}(t)$ in SABS region i at any instant t was given by the following function (Antonopoulos and Gianniou 2003; Thomann and Mueller 1987):

$$\theta_{i_A} = \alpha_{OP} \mu_{i,k_Ts}(t) (1.066)^{T(t)-20} e^{-\frac{\tau}{2\sigma^2} Cc A_{i,k}(t)}, \tag{12}$$

where α_{OP} is the Chla-oxygen utilization ratio ($\text{mg-O}_2 \text{ L}^{-1} \text{ day}^{-1}$), τ is calculated as $\frac{(K_a A_{i,k}(t) Cc + K_r)z}{\log(2)}$, and σ is calculated as $\frac{\log(\frac{2I_o(H)}{a})}{\log(2)} \sqrt{\frac{2}{\pi}}$, and all other parameters are as previously described.

The respiration rate ($\text{mg-O}_2 \text{ liter}^{-1} \text{ day}^{-1}$) of phytoplankton species $A_{i,k}(t)$ at any instant t was given by the following function (Thomann and Mueller 1987):

$$\theta_{i,k_r} = K_{\text{resp}} (1.08)^{T-20} Cc A_{i,k}(t), \tag{13}$$

where K_{resp} is the combined respiration rate, equal to $\alpha_{OP} * K_r$, where K_r is the respiration rate coefficient (day^{-1}).

The oxygen exchange rate ($\text{mg-O}_2 \text{ L}^{-1} \text{ day}^{-1}$) between the atmosphere and surface water was a function of the DO concentration and temperature, given by

$$\theta_{i_d} = DO_{\text{sat}}(t) - DO_i(t) d_{\text{flux}}, \tag{14}$$

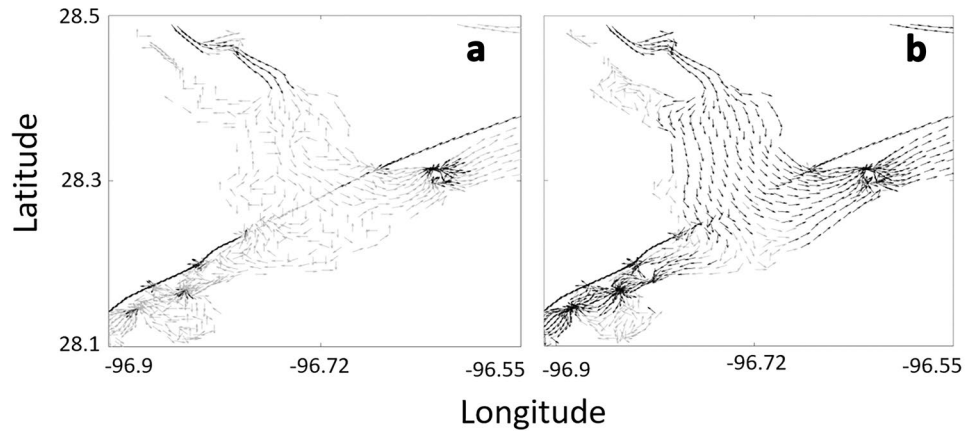
where $DO_{\text{sat}}(t)$ was DO saturation at the subsurface equal to $e^{7.7117 - 1.31403 \ln(T+45.93)}$ (Michaud 1991; Moore 1989; Mortimer 1981), $DO_i(t)$ was the DO concentration in region i at instant t , and d_{flux} was the molecular diffusion rate (day^{-1}).

Physical Modeling Framework

Simulations involving model training were run using flow vectors generated by Texas Water Development Board’s (TWDB) TxBLEND model. TxBLEND simulation domains that encompassed SABS over a time span from 1987 to 2013 with a daily time step generated the velocity components of water movement decomposed into the N-S and E-W vectors (Fig. 2).

Boundary lines between segments of the SABS in our model’s physical domain were determined from previous analyses (Roelke et al. 2017). The slope of these boundary lines influenced translation of TxBLEND flows into water exchanges between segments. For example, in the SABS, the boundary line between upper and middle SABS zones was horizontal (east–west direction, Fig. 3a). Therefore, we chose only the north–south velocity components from the TxBLEND model to determine the direction of net flow. But the boundary line between the middle and lower SABS patches makes an angle $\theta_{ML} (\sim 36.5^\circ)$ to the east (Fig. 3a). The resultant velocity component (R_{ML}) perpendicular to boundary between patches is

Fig. 2 Circulation in the San Antonio Bay System (SABS), as estimated using the Texas Water Development Board’s TxBLEND model. Representative days are shown during a period of low river discharges (a) and high river discharges (b), where gray arrows indicate velocities < 0.1 ft/s and black arrows indicate velocities > 0.1 ft/s



$$R_{ML} = \begin{cases} \sqrt{N_c^2 + W_c^2} \cos \psi_{NW}, & \text{for NW - direction} \\ \sqrt{S_c^2 + W_c^2} \cos(\theta_{ML} + \phi_{SW}), & \text{for SW - direction} \\ \sqrt{N_c^2 + E_c^2} \cos(\theta_{ML} + \phi_{NE}), & \text{for NE - direction} \\ \sqrt{S_c^2 + E_c^2} \cos(\theta_{ML} + \phi_{SE}), & \text{for SE - direction,} \end{cases} \quad (15)$$

where $N_c, S_c, E_c,$ and W_c were the TxBLEND generated water velocity components along the $N, S, E,$ and W directions respectively, $\psi_{NW} = \theta_{ML} \cos^{-1}\left(\frac{N_c}{\sqrt{N_c^2 + W_c^2}}\right), \phi_{SW} = \cos^{-1}\left(\frac{S_c}{\sqrt{S_c^2 + W_c^2}}\right), \phi_{NE} = \cos^{-1}\left(\frac{N_c}{\sqrt{N_c^2 + E_c^2}}\right),$ and $\phi_{SE} = \theta_{ML} \cos^{-1}\left(\frac{S_c}{\sqrt{S_c^2 + E_c^2}}\right).$ We obtain velocity components for the other angular boundaries (lower SABS-Espiritu Bay and lower SABS-Mesquite Bay) by using a similar approach.

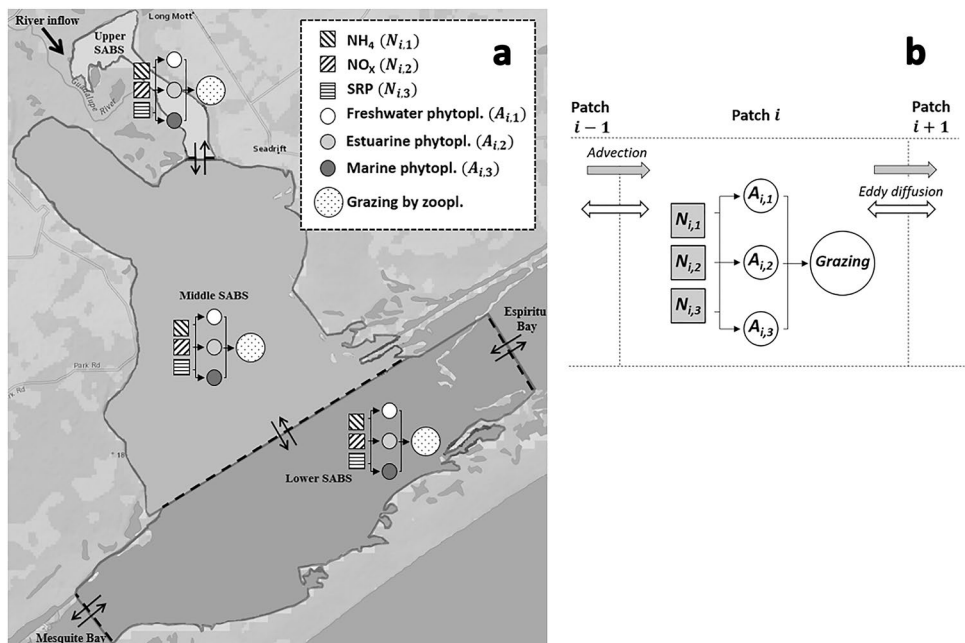
The volume of water per unit time moving across a boundary line is simply the average water velocity perpendicular to the boundary line multiplied by the boundary’s cross-sectional area, i.e., width \times depth. The bay region-specific hydraulic flushing rate, $D,$ is this water volume per unit time value, divided by the volume of the bay segment in question. For example, the hydraulic flushing rate for the middle SABS attributed to water exchanges with the lower SABS is

$$D_{M,ML} = \frac{|R_{ML}| \times \text{width} \times \text{depth of boundary}_{ML}}{\text{volume of region}_M} \quad (16)$$

and the hydraulic flushing rate for the lower SABS attributed to water exchanges with the middle SABS is

$$D_{L,ML} = \frac{|R_{ML}| \times \text{width} \times \text{depth of boundary}_{ML}}{\text{volume of region}_L} \quad (17)$$

Fig. 3 Conceptual diagram of the modeling framework for the San Antonio Bay MUMPS model. The physical scheme (a) was comprised of three patches (or regions) between which advection and eddy diffusion processes moved nutrients and phytoplankton cells. The biological reaction scheme (b) was embedded within each model bay region and was comprised of three resources, i.e., $\text{NH}_4 (N_{i,1}), \text{NO}_x (N_{i,2}),$ and $\text{SRP} (N_{i,3});$ three phytoplankton groups, i.e., freshwater ($A_{i,1}$), estuarine ($A_{i,2}$), and marine ($A_{i,3}$); grazing by zooplankton; and light effects (not shown)



For the upper SABS, the total D was based on river discharge and water exchanges between the upper and middle SABS. For the middle SABS, the total D was based on water exchanges between the upper and middle SABS and the middle and lower SABS. For the lower SABS, the total D was based on water exchanges between the middle and lower SABS, the lower SABS and Espiritu Bay, and the lower SABS and Mesquite Bay.

Coupled Biophysical Modeling Frameworks and Differential Equations

As described in the previous section, the biophysical framework of the SABS model consisted of three connected patches or regions, representing the three subdivisions of the SABS. Freshwater inflows enter the model domain through the uppermost region, and water exchanges with marine end-members occur in the lower-most region (Fig. 3a). Within each region, phytoplankton compete for three growth-limiting resources, also described in a previous section (Fig. 3b). In the uppermost region of SABS, advection from rivers brings nutrients and cells (freshwater species only) into the model domain. Water exchanges between SABS regions transfer cells and nutrients throughout the model domain and also between adjacent systems and the lower SABS (Espiritu and Mesquite Bays). The input of freshwater phytoplankton cells from the rivers was given by

$$\text{Cells}_{\text{Rivers}}^F = \frac{\text{River Chla} \times \text{River Inflow}}{C_c \times \text{Volume of Upper SABS}} (\times 10^6 \text{ cells L}^{-1} \text{ day}^{-1}) \tag{18}$$

where *River Inflow* was the daily-averaged freshwater discharges from the Guadalupe and San Antonio Rivers and C_c was the chlorophyll per phytoplankton cell ($\mu\text{g-Chla}/10^6$ cells, calculation as previously described). The input of estuarine and marine phytoplankton cells from Mesquite and Espiritu Bays was given by

$$\text{Cells}_{\text{Bays}}^{\text{EM}} = \frac{\text{Adjacent Bay Chla}}{2 \times D \times C_c} (\times 10^6 \text{ cells L}^{-1} \text{ day}^{-1}) \tag{19}$$

For subdivisions of the SABS, if there was a flow from region i , towards region $i + 1$, influencing region i , where the upper SABS was $i = 1$, the middle SABS $i = 2$, and the lower SABS $i = 3$, then the differential equations for phytoplankton and nutrients in region i follow the forms

$$\frac{dA_{i,k}}{dt} = A_{(i,k)} \{ \mu_{(i,k)} - D_{i,i+1,i} - g_i \} + A_{i-1,k} D_{i-1,i,i} \tag{20}$$

$$\frac{dN_{i,j}}{dt} = N_{i-1,j} D_{i-1,i,i} - N_{i,j} D_{i,i+1,i} - \sum_k Q_{N_{i,j,k}} \mu_{i,k} A_{i,k}, \tag{21}$$

where $A_{i,k}$ was the k^{th} phytoplankton species in patch i , $N_{i,j}$ was the j^{th} nutrient in patch i , and $Q_{N_{i,j,k}}$ was the fixed cellular content of resource $N_{i,j}$ in species k .

The rate of change DO in any given patch at any instant t was given by

$$\frac{d(\text{DO}_i)}{dt} = A_{i,k} (\theta_{i,k,A} - \theta_{i,k,R}) + \theta_{i,d} \text{DO}_i \tag{22}$$

We employed numerical techniques to solve the spatially discrete differential equations using MATLAB-ODE-solving routines based on fourth-order Runge–Kutta procedures with a variable time step. The daily averaged data were used in the output figures reported as part of this work.

Model Training

Historical data from Roelke Lab (described above and reported in Roelke et al. 2017) was used for model training. For the training, we employed a parsed approach to parameter manipulation. We first optimized the model to the data through manipulation of the temperature- and salinity-based parameters (described below). Then, we further optimized the model to the data through manipulation of parameters related to light, grazing, and nutrient use (described below). In each of the bay areas, performance of the model with each parameter manipulation was quantified using the statistical metric, root-mean-square error (RMSE). The RMSE can be calculated as

$$\text{RMSE} = \sqrt{\frac{1}{T} \sum_{t=1}^T [S(t) - O(t)]^2}, \tag{23}$$

where T is the length of observations, and $O(t)$ and $S(t)$ are field observations and model simulation results respectively at time t ($t = 1, 2, \dots, T$). For the RMSE calculation, we used Chla and DO. We then summed the three RMSE values from the three bay regions. We show field observations and model results for Chla and DO.

For the first step in the model training, three Q10 values were explored for all of the salinity-based parameter manipulations. These Q10 values were 1, 2, and 3. For the salinity-based parameters, ranges for the maximum salinity tolerance, optimal salinity, and minimum salinity tolerance were explored for each of the three phytoplankton groups. For the freshwater phytoplankton species, the range for maximum salinity tolerance was [10, 25]; for the estuarine phytoplankton species, the ranges for the maximum salinity tolerance, optimal salinity, and minimum salinity tolerance were [20, 35], [5,19], and [0, 4] respectively; for the marine phytoplankton species, the ranges for the maximum salinity tolerance and minimum salinity tolerance were [35, 50] and [5–20] respectively. The

RMSE values with $Q10 = 3$ were much better than the corresponding RMSE values obtained using $Q10 = 1$ and $Q10 = 2$. The salinity-based parameters that produced the best RMSE at $Q10 = 3$ were $s_{max}^F = 10$ ppt, $s_{max}^E = 20$ ppt, $s_{max}^M = 35$ ppt, $s_{opt}^E = 19$ ppt, $s_{min}^E = 4$ ppt, and $s_{min}^M = 20$ ppt.

For the second step in the model training, we considered a combination of six optimization orders (OP_i) based on the parameters that were grouped into light (K_t), grazing ($g_{max}, s_{min}^g, s_{opt}^g, s_{max}^g$), and NH_4/NO_x preference (γ). We followed this approach in lieu of global optimization because of computational limitations. The order in arrangements of the parameters was as follows:

$$OP_1 = \{K_t, g_{max}, s_{min}^g, s_{opt}^g, s_{max}^g, \gamma\}$$

$$OP_2 = \{K_t, \gamma, g_{max}, s_{min}^g, s_{opt}^g, s_{max}^g\}$$

$$OP_3 = \{g_{max}, s_{min}^g, s_{opt}^g, s_{max}^g, K_t, \gamma\}$$

$$OP_4 = \{g_{max}, s_{min}^g, s_{opt}^g, s_{max}^g, \gamma, K_t\}$$

$$OP_5 = \{\gamma, g_{max}, s_{min}^g, s_{opt}^g, s_{max}^g, K_t\} \text{ and}$$

$$OP_6 = \{\gamma, K_t, g_{max}, s_{min}^g, s_{opt}^g, s_{max}^g\}$$

The lowest RMSE values resulted from OP_3 (Table 1). These parameters were then used in the sensitivity and simulation analyses Table 2.

Sensitivity and Simulation Analyses

The sensitivity analysis focused on changes in model output for average Chla and DO during spring and summer, resulting from either an increase or decrease (50% of the optimized value for a particular parameter). Results were similar across

bay regions; therefore, we show results for only the middle SABS region, where trends were most pronounced.

The simulation analysis for the SABS comprised an evaluation of phytoplankton biomass (as Chla) and DO in the system over a range of river inflows and nutrient loadings. For this, we generated an annual hydrological cycle that delivered a yearly inflow magnitude comparable to that of the 27-year daily-averaged data set (data described in a previous section). This “historical average” was then increased or decreased across a range of 0–2 times the original magnitude to create different levels of river discharge. A similar process was used for river nutrient loading. However, river nutrient samplings in the 27-year data set were sparse during some periods; therefore, monthly averages were generated across the 27-year period. These monthly averages were interpolated to create a daily data set.

Each of the combined inflow and river nutrient concentration-combination simulations were repeated using low (0.2 d^{-1}), medium (1.0 d^{-1}), and high (2.0 d^{-1}) eddy diffusion rates for the upper SABS (d_U). We opted to use this simpler approach for depicting eddy diffusion instead of using the seasonally varying water exchange rates estimated with TxBLEND, as this kept interpretation of our model results tractable. In the upper region of the SABS, diffusive exchanges occurred only with the middle region. In the middle region of the SABS, diffusive exchanges occurred with both the upper and lower regions. In the lower region of the SABS, diffusive exchanges occurred with the middle region and two adjacent bay systems (marine end-members). To determine eddy diffusion in the middle ($d_{M,L}$) and lower ($d_{M,L}$) SABS regions, we used the following equations:

$$d_{M,L} = \frac{d_U \times \text{Volume of region}_U}{\text{Volume of region}_{M,L}}, \tag{24}$$

In order to incorporate eddy diffusion rates (d_i) explicitly, we added terms to differential Eqs. (20) and (21) which differed depending on the bay region. For the upper SABS region, the terms took the form $(A_{i+1,k} - A_{i,k})d_i$ and $(N_{i+1,j} - N_{i,j})d_i$. For the

Table 1 Results from model optimization where root-mean-square error (RMSE) was used to evaluate deviations between the field data from the Roelke Lab and the model simulation values in the upper, middle, and lower regions of the San Antonio Bay System (USABS, MSABS, and LSABS, respectively). The order in which parameter

values were adjusted varied, as this influenced how well the model was optimized. The parameters adjusted were related to light (K_t), grazing ($g_{max}, s_{min}^g, s_{opt}^g, s_{max}^g$), and NH_4/NO_x preference (γ). There were six parameter sequences explored, designated with $OP_1, OP_2, OP_3, OP_4, OP_5,$ and OP_6

Order	Optimized parameter values						RMSE		
	K_t	g_{max}	s_{min}^g	s_{opt}^g	s_{max}^g	γ	USABS	MSABS	LSABS
OP_1	0.97	0.03	0.65	1	28	0.61	9.72	12.52	21.32
OP_2	0.97	0.03	0.7	0.75	27	0.06	9.75	12.52	21.31
OP_3	0.45	0.03	0.65	1	27	0.88	11.84	9.68	20.85
OP_4	0.4	0.03	0.65	1	27	0.19	12.05	10.01	20.89
OP_5	0.47	0.07	0.7	1.1	32	0.34	11.38	10.24	20.83
OP_6	0.99	0.035	0.7	0.8	29	0.34	9.55	12.63	21.34

Table 2 Parameters of the model defined with values, units, and references shown where appropriate

Group	Parameter	Description	Value	Unit	Reference
Nutrient	NH ₄	Ammonia		μg L ⁻¹	
	NO _X	NO ₂ /NO ₃		μg L ⁻¹	
	SRP	Soluble reactive phosphorous		μg L ⁻¹	
Phytoplankton	r*	Maximum specific growth rate	1.0	Day ⁻¹	Withrow et al. (2018)
	μ _{Ts}	Growth rate limited by temperature and salinity		Day ⁻¹	Eppley (1972)
	μ _N	Specific growth rate on nitrogen		Day ⁻¹	
	μ _P	Specific growth rate on phosphorous		Day ⁻¹	
	μ _L	Specific growth rate on light		Day ⁻¹	
	μ _i	Specific growth rate (minimum of resource limited rates)		Day ⁻¹	
	K _N *	Half saturation coefficient growing on nitrogen	0.5	μg L ⁻¹	Redfield (1934)
	K _P *	Half saturation coefficient growing on phosphorous	0.0313	μg L ⁻¹	Redfield (1934)
	a	Half saturation coefficient growing on light	μ _{max} × 0.203 × 10 ²⁰	Quantacm ⁻² s ⁻¹	Huisman (1999)
	Q _N *	Fixed cellular content for nitrogen	0.1575	μg 10 ⁻⁶ cells	Mullin et al. (1966)
	Q _P *	Fixed cellular content for phosphorous	0.0098	μg 10 ⁻⁶ cells	Mullin et al. (1966)
	s _{min} ^E *	Minimum sustainable salinity threshold (estuarine phytoplankton)	4	psu	User defined
	s _{min} ^M *	Minimum sustainable salinity threshold (marine phytoplankton)	20	psu	User defined
	s _{opt} ^E *	Optimum salinity threshold (estuarine phytoplankton)	19	psu	User defined
	s _{max} ^F *	Maximum sustainable salinity threshold (freshwater phytoplankton)	10	psu	User defined
	s _{max} ^E *	Maximum sustainable salinity threshold (estuarine phytoplankton)	20	psu	User defined
	s _{max} ^M *	Maximum sustainable salinity threshold (marine phytoplankton)	35	psu	User defined
	C _C *	Chlorophyll-to-carbon ratio in phytoplankton	0.012	--	Mullin et al. (1966)
	V	Cellular volume	64π/3	μm ³	
	θ _A	Oxygen production rate by phytoplankton		mg-O ₂ L ⁻¹ day ⁻¹	Thomann and Mueller (1987)
θ _r	Respiration rate of phytoplankton		mg-O ₂ L ⁻¹ day ⁻¹	Thomann and Mueller (1987)	
K _{resp} *	Combined respiration rate	0.125	μg-O ₂ (μg-Chla) ⁻¹ day ⁻¹	Thomann and Mueller (1987)	
K _r	Coefficient of respiration rate	1.25	Day ⁻¹	Thomann and Mueller (1987)	
α _{OP} *	Ratio of Chla to oxygen utilized	0.1	μg-O ₂ (μg-Chla) ⁻¹	Antonopoulos and Gianniu (2003), Thomann and Mueller (1987)	
Zooplankton	γ*	NH ₄ :NO _X utilization ratio	0.88	--	Optimization
	g _{max} *	Maximum grazing rate	0.03	Day ⁻¹	Optimization
	s _{min} ^g *	Minimum sustainable salinity for grazing	0.65	psu	Optimization
	s _{opt} ^g *	Optimum salinity for grazing	1	psu	Optimization
	s _{max} ^g *	Maximum sustainable salinity for grazing	27	psu	Optimization

Table 2 (continued)

Group	Parameter	Description	Value	Unit	Reference
Light	$I_o(H)$	Hourly incident light intensity			Brock (1981)
	I	Daily integrated solar radiation			Brock (1981)
	W_1	Sunset hour angle		Radians	Brock (1981)
	K_a^*	Light attenuation coefficient on based on Chla	0.0024	$\text{dcm}^2(\mu\text{g-Chla})^{-1}$	Olivieri and Chavez (2000)
	K_t^*	Light attenuation coefficient of water	0.45	dcm^{-1}	Optimization
Other	s	Salinity		psu	
	DO_{sat}	Saturated oxygen at the subsurface		$\text{mg-O}_2 \text{L}^{-1}$	Michaud (1991)
	c	Fraction of mean cloud cover per day	0.1	--	Brock (1981)
	L	The latitude of southern coast of Texas	30	Degree	Study system location
	d_{flux}^*	Molecular diffusion rate	2.1	Day^{-1}	Michaud (1991), Moore (1989), Mortimer (1981)
	q	Q10 values	2–3	--	User defined
	T	Temperature		$^{\circ}\text{C}$	
	H	Time of the day		Hour	
	$Cells_{Rivers}^F$	Input of phytoplankton cells from the rivers		$10^6 \text{cellsL}^{-1} \text{day}^{-1}$	Roelke et al. (2017)
	$Cells_{Bays}^{EM}$	Input of phytoplankton cells from marine end-members		$10^6 \text{cellsL}^{-1} \text{day}^{-1}$	Gable (2010), Roelke et al. (2017)
	$D_{x,y,z}$	Flushing rate at the boundary between the patches x and y impacting on patch z		Day^{-1}	TxBLEND simulation
	R_x	Average flow velocity in patch \times perpendicular to the boundary		dcm day^{-1}	TxBLEND simulation

*Parameters used as part of the sensitivity analysis

middle SABS, the terms took the form $(A_{i+1,k} + A_{i-1,k} - 2A_{i,k})d_i$ and $(N_{i+1,j} + N_{i-1,j} - 2N_{i,j})d_i$. For the lower SABS, the terms took the form $(A_{i+1,k} + A_{i+1,k} + A_{i-1,k} - 3A_{i,k})d_i$ and $(N_{i+1,j} + N_{i+1,j} + N_{i-1,j} - 3N_{i,j})d_i$. For the lower SABS, region $i + 1$ represents the adjacent bay systems.

Results

Model Training

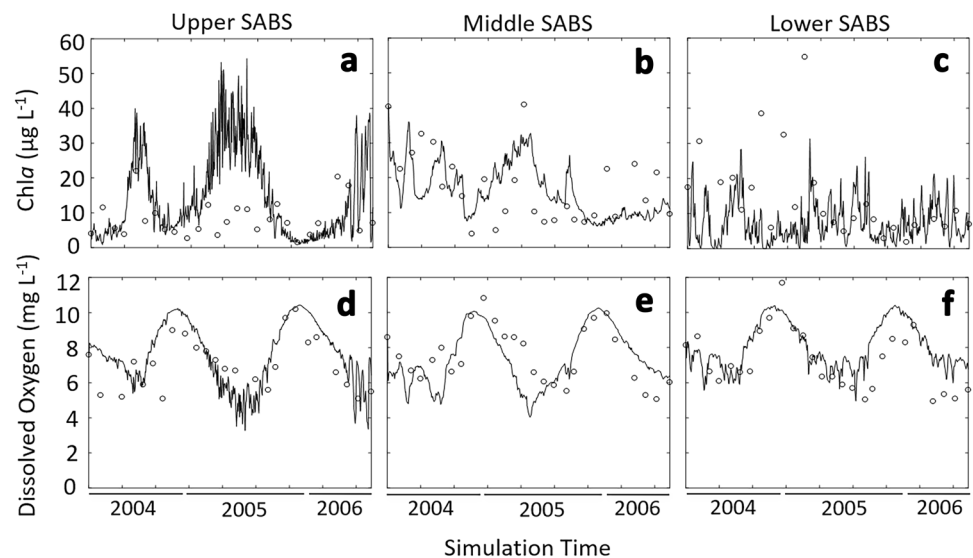
In all three regions of SABS, the model reproduces DO concentration well, capturing the timing and magnitude of fluctuations (Fig. 4d–f). Differently, while model results for Chla concentration are primarily within the range of historical values, they are often out of sync with the timing and magnitude of fluctuations, especially in the upper SABS region (Fig. 4a–c).

Sensitivity Analyses of the SABS

These analyses revealed that Chla during the spring months in SABS was particularly sensitive to changes in maximum phytoplankton growth rate (r), phytoplankton cellular quota for phosphorous (Q_p), Chla:C-ratio, maximum grazing rate (g_{max}), turbidity coefficient (K_t), and maximum salinity threshold for grazing (s_{max}^g) (Fig. 5a). With the exception of “ r ”, Chla was sensitive to these same parameters in the summer (Fig. 5b).

In regard to DO, during spring months in the SABS, the model was remarkably insensitive to changes in any of the parameters tested (Fig. 5c). During the summer months, the same parameters that were important for Chla prediction were also important for DO (but less so). In addition, the model was sensitive to changes in O_2 -diffusion coefficient (d_{flux}), the Chla- O_2 conversion parameter (α_{OP}), and the phytoplankton respiration coefficient (K_{resp}) (Fig. 5d).

Fig. 4 San Antonio Bay MUMPS results after model training, where data from the Roelke laboratory at Texas A&M University Galveston (open circles) and simulation results (solid lines) are superimposed. Results are shown for chlorophyll *a* (Chla, **a–c**) and dissolved oxygen (**d–f**) in the upper (**a, d**), the middle (**b, e**), and the lower (**c, f**) regions of the SABS



Simulation Analyses of the SABS

In all three regions of the SABS, annual biomass (Chla multiplied by bay segment volume for each day of the year, then summed for the year) increased with an initial decrease in river inflows from the historical condition; a response was most exaggerated at the lowest levels of eddy diffusion (Fig. 6). While similar in trend, the annual biomass in the upper, middle, and lower regions increased to different extents. In the upper region, annual biomass reached its maximum (under average nutrient conditions) at 2.0×10^{14} mg Chla when inflows were reduced to 20% of the historical average. This was a 90.7% increase in annual biomass from the average condition of 1.07×10^{14} mg Chla. In the middle region, annual biomass reached a maximum at 9.12×10^{15} mg Chla, when inflows were reduced to 40%, generating a 36.5% increase from the average condition of 6.68×10^{15} mg Chla. In the lower region, Chla reached a maximum at 6.23×10^{14} mg Chla, when inflows were reduced to 60%, a 14.9% increase from the average condition of 5.42×10^{15} mg Chla. The response was weakest at the highest levels of eddy diffusion (Fig. S1). As river inflows decreased to zero, biomass decreased to its minimum, resembling the marine boundary conditions. Differently, when river inflows were increased from the historical condition, biomass in all three regions decreased, eventually approaching a value similar to the river boundary condition.

Regarding nutrient loading at typical river inflows in SABS, appreciable reductions in annual biomass were not observed until nutrient concentrations in the river were less than 60% of the average condition (Fig. 6). This result was consistent at all three levels of eddy diffusion. When river inflows were high, annual biomass became less sensitive to changes in the concentration of nutrients in the river. Differently, when river inflows were low, annual biomass

became sensitive to reductions in river nutrient concentrations, showing a corresponding decrease, and the decrease was greater as inflows were further reduced. The response was again most exaggerated at the lowest levels of eddy diffusion, where the annual biomass at the averaged nutrient concentration in the river (but lower flow at 20% of the historical average) decreased to different extents in each region. The upper, middle, and lower regions decreased from 1.79×10^{14} , 9.12×10^{15} , and 4.77×10^{15} mg Chla, respectively, to 1.15×10^{14} , 4.94×10^{15} , and 1.18×10^{15} mg Chla, respectively, when nutrients were reduced to 40% of their historical average. This corresponds to annual biomass decreases of 35.8%, 45.8%, and 61.6% in the upper, middle, and lower regions respectively.

Annual biomass was comprised of three phytoplankton populations in each region, which were influenced differentially by salinity. Figure 7 is shown as an example of the shift in population abundances as freshwater inflows are shifted away from the average condition. Under the average condition, with Fig. 6 surface plot coordinates of (1,1), both the freshwater and estuarine populations contribute to annual biomass in the region. At the extreme end of freshwater inflows where the average condition is doubled, indicated by Fig. 6 surface plot coordinates of (2,2) to (2,0), the freshwater population is the primary contributor to annual biomass. At the other discharge extreme, where no inflow occurs, only a small estuarine population persists in the region. Comparison of the bottom three panels of Fig. 7 shows how the assemblage shifted from primarily estuarine to co-dominance by freshwater and estuarine groups as discharge was increased across average nutrient conditions, indicated by Fig. 6 surface plot coordinates of (0.4,1), (1,1), and (1.6,1).

Dissolved oxygen responses to changing river inflows and nutrient loadings in the SABS varied by region (Fig. 8). Across all three regions, the yearly minimum DO

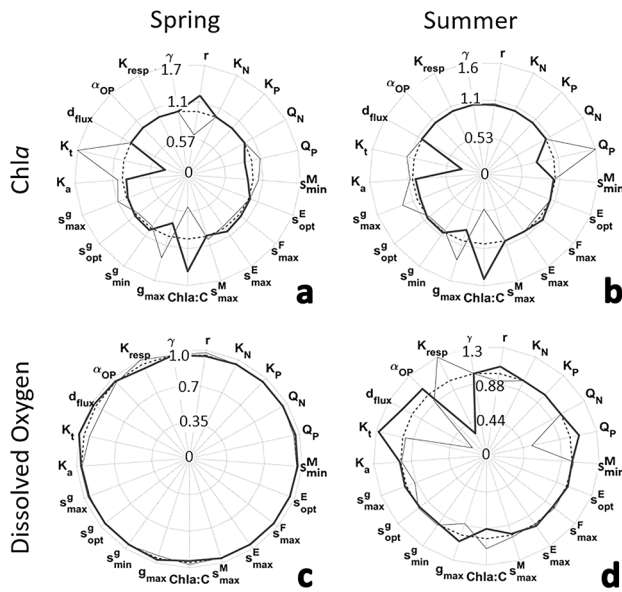


Fig. 5 Sensitivity of the middle region of the San Antonio Bay System (SABS) MUMPS to changes in model parameters. Responses were similar across bay regions. MUMPS response variables for chlorophyll *a* (a, b) and dissolved oxygen (c, d) were analyzed in the spring (a, c) and summer (b, d) months. Model responses using the default parameter values are shown by a dashed line (always in the shape of a circle and with a value of 1.0). Model responses from simulations where an individual parameter was manipulated are shown by either a thin, solid line (−50%) or a thick, solid line (+50%). The scaling of the maximum polar coordinates (outer circle of graphic) varies between panels as shown; e.g., panel a is scaled to a maximum factor of 1.7, with inner circles at 1.1 and 5.7. Model responses with values greater than 1.0 indicate an increase from the response generated using the default value, and responses with values less than 1.0 indicate a decrease. Phytoplankton parameter identifications include chlorophyll *a* to oxygen utilization ratio (α_{OP}), coefficient of respiration rate (K_{resp}), $\text{NH}_4\text{:NO}_x$ preference ratio (γ), maximum growth rate (r), half-saturation coefficient for combined NH_4 and NO_x (K_N), half-saturation coefficient for SRP (K_P), fixed cellular content of nitrogen (Q_N), fixed cellular content of phosphorus (Q_P), marine group minimum salinity threshold (s_{min}^M), estuarine group optimum salinity threshold (s_{opt}^E), freshwater group maximum salinity threshold (s_{max}^F), estuarine group maximum salinity threshold (s_{max}^E), marine group maximum salinity threshold (s_{max}^M), and chlorophyll *a* to carbon ratio (Chl*a*:C). Non-phytoplankton parameter identifications include maximum grazing rate (g_{max}), minimum salinity for grazing (s_{min}^g), optimum salinity for grazing (s_{opt}^g), and maximum salinity for grazing (s_{max}^g), mass-based light-attenuation coefficient of phytoplankton (K_a), background turbidity (K_t), and atmosphere-water diffusion rate for oxygen (d_{flux})

was primarily influenced by discharge level. In the upper SABS, minimum DO increased with decreasing discharge and decreased with an initial increase in discharge to a certain point (~60% of average condition), where minimum DO again began to increase. Minimum DO in the upper SABS ranged from 6.4 to 8.4 mg L^{−1}. Differently, in the middle and lower SABS regions, yearly minimum DO primarily decreased with increasing flows, ranging from 5.4 to 8.0 mg

L^{−1}. As with Chl*a*, this result was consistent at all three levels of eddy diffusion (Fig. S2). The annual average DO mirrored trends for minimum DO in each bay region, but with much less amplitude where maxima and minima were in the ranges of ~9.5 mg L^{−1} and ~7.75 mg L^{−1}, respectively (Fig. S3).

Discussion

At the historically averaged river inflow condition, phytoplankton reproductive growth rate in SABS appears to be controlled primarily by light, as suggested by our model findings. This is evidenced by little to no effect on annual biomass with the increase of nutrient concentrations in the river. Recall that for some simulation comparisons, nutrient loading changes occurred independent of hydraulic displacement changes (i.e., inflow was held constant). With the model simulations under constant cell displacement rates, increased nutrients should allow for increased reproductive growth rate, assuming nutrients are limiting, and an increase in population growth. However, no increase occurred, pointing to resource limitation by another model factor, in this case, light. A previous model, focused on induction of photosynthesis, also proposed light as the controlling factor for biomass in the SABS (MacIntyre and Geider 1996). In addition, these findings suggest that the impact of increased nutrient loading in the SABS is likely beyond the domain of the current model (i.e., further away from the locations of discharge of these rivers), similar to other bay systems in this region (Chen et al. 2000).

When inflows were increased beyond the historical average, annual biomass was reduced due to increased hydraulic displacement of cells, which reduced the population growth rate. Phytoplankton reproductive growth rate in the SABS remained primarily light-limited at these higher river inflows.

Differently, when inflows were reduced below the historical average, annual biomass increased substantially. This occurred because population growth rate was enhanced with the reduced hydraulic displacement of cells, enabling greater accumulation of cells. At these lower inflows, river nutrient concentrations were more influential in determining annual biomass. Interestingly, as inflows were further reduced, nutrient reductions became more impactful on annual biomass. Under extreme low-inflow conditions, changes in annual biomass were positively correlated with river nutrient concentrations across all nutrient loading levels. This effect was most severe in the upper SABS region and least severe in the lower SABS region. This suggests that under diminished inflow conditions, nutrient reductions may be important for the control of phytoplankton growth and maintenance of biomass.

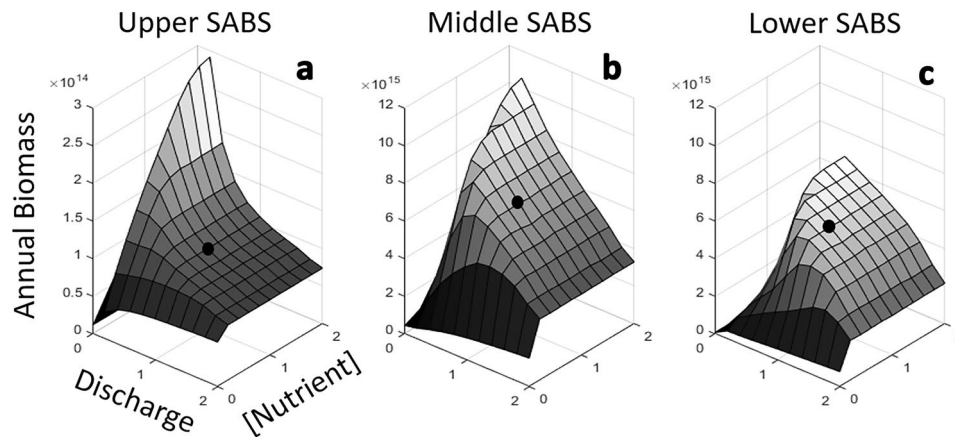


Fig. 6 San Antonio Bay System (SABS) MUMPS model simulated annual biomass (daily chlorophyll *a* concentration multiplied by the SABS region volume, then summed over the course of the year) as a function of river discharge and nutrient concentrations. Results are shown for the upper (a), middle (b), and lower (c) SABS regions. The

x- and *y*-axes are multipliers of the average annual hydrology and nutrient concentrations in the river, where a value of “1” represents the 27-year average inflow and nutrient concentrations in the river. Results generated under the average conditions are indicated with a black dot

Yearly minimum DO was highly influenced by river discharge levels and, in most cases, relatively insensitive to changes in river nutrient concentrations. The effect of discharge on model DO was indirect; phytoplankton biomass and physiological state were directly influenced by inflows, which in turn impacted DO. This relationship led to variation in DO trends between bay regions based on their salinity at different discharge levels. Simulated oxygen production by model phytoplankton was, in part, a function of their maximum potential growth rate, as determined by temperature and salinity. Under high discharge conditions, phytoplankton input from the river (freshwater population) was high, salinity was low, and the freshwater population was able to grow near its maximum in the upper SABS. As a portion of the freshwater population was pushed further into the bay via advection, it encountered higher salinity and reduced growth rate. So, although the freshwater population contributed to Chl*a* in the middle and lower SABS regions, because their growth was diminished, their contribution to DO was greatly reduced, and their continued respiration led to a net loss for DO. Under low biomass conditions, where the phytoplankton contribution to DO was minimal, oxygen re-entry from the atmosphere was sufficient to maintain DO throughout SABS.

We can compare these results to the findings of Hu et al. (2020), where high discharge to the SABS occurred following Hurricane Harvey and led to decreased Chl*a* and DO within the system. The decrease in Chl*a* was attributed to increased turbidity, inhibiting primary production, while the decrease in DO was attributed to an increase in organic carbon and subsequent elevated microbial respiration. Though MUMPS does not yet incorporate processes related to variable turbidity or bacterial respiration, it is

likely that processes attributing to the model results for the middle and lower SABS also influenced the empirical observations reported by Hu et al. (2020) to some degree (i.e., the hurricane-related discharge leads to the increased flushing of phytoplankton biomass which contributed to the decrease in Chl*a* and oxygen reductions). Walker et al. (2021) also reported a marked decrease in DO and Chl*a* in the SABS following Hurricane Harvey. Interestingly, when river discharge was reduced, a regional shift in biomass occurred with the middle SABS becoming more prominent than the lower SABS. For example, in the middle region of the SABS, biomass increased 36.5%, while in the lower SABS, biomass increased 14.9%. This resulted in the middle SABS having ~46% more biomass than the lower SABS, a change from ~23%. These modeling results parallel what has been observed in field monitoring for this system, where it was shown that under prolonged low-inflow conditions, the biomass “hot spot” forms in the middle SABS (Roelke et al. 2017). The impact of a regional shift in phytoplankton biomass of this magnitude on sessile organisms (e.g., oysters), organisms of limited dispersal (e.g., juvenile blue crabs), or the organisms that feed on these (e.g., endangered whooping cranes for the case of blue crabs) merits further study, as possible effects on higher trophic levels are unclear.

Findings from our sensitivity and simulation analyses point to areas of further model refinement that may increase the accuracy of the model. For example, Chl*a* during the spring and summer months in SABS was sensitive to changes in the Chl*a*:C-ratio. In our current modeling efforts, the ratio was kept constant. In reality, this ratio is different among phytoplankton taxa, and it changes with their physiological state (Letelier et al. 1993; Brewin et al. 2019). Using taxon-specific Chl*a*:C-ratios and incorporating mechanisms

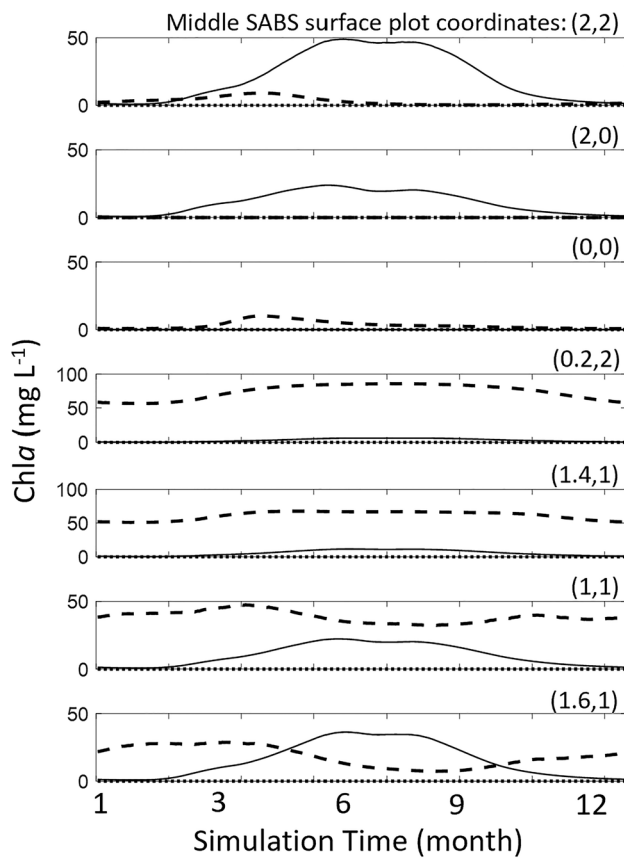


Fig. 7 San Antonio Bay System (SABS) MUMPS model time-series simulation results for Chl *a* in the middle region. Coordinates above the upper right corner of each plot represent the *x*- and *y*-axes for a given sim on the surface plot found in Fig. 6. The coordinates are multipliers of the average annual hydrology and nutrient concentrations in the river, respectively, where a value of “1” represents the 27-year average inflow and nutrient concentrations in the river. The solid line represents the freshwater phytoplankton population, the dashed line represents the estuarine population, and the dotted line represents the marine population

in the model that simulate changes in this ratio with physiology may improve Chl *a* predictions.

Similarly, Chl *a* during the spring and summer months in SABS was sensitive to changes in the turbidity coefficient (K_t). As with the Chl *a*:C-ratio, K_t was kept constant in our modeling effort. In reality, K_t changes with loading of colored dissolved organic matter (CDOM) and detritus (Babin et al. 2003; Rose et al. 2019). We are unaware of studies along the Western Gulf coast focusing on the changed optical properties of bay waters as a result of CDOM and detritus loading. Such a study, however, would enable these influences to be incorporated in the model, possibly leading to improved Chl *a* predictions.

The maximum growth rate of phytoplankton (r), maximum salinity threshold for grazing (s_{\max}^g), and the maximum grazing rate (g_{\max}) also had a large influence on Chl *a* during

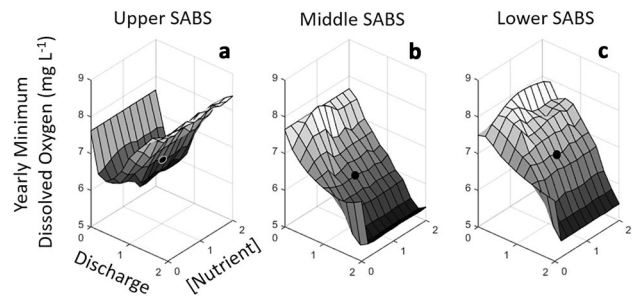


Fig. 8 San Antonio Bay System (SABS) MUMPS model simulated minimum dissolved oxygen as a function of river discharge and nutrient concentrations. Results are shown for the upper (a), middle (b), and lower (c) SABS regions. The *x*- and *y*-axes are multipliers of the annual hydrology and nutrient concentrations in the river, where a value of “1” represents the 27-year average inflow and nutrient concentrations in the river. Results generated under the average conditions are indicated with a black dot

the spring and summer months in SABS. As with the parameters mentioned above, they were also kept constant in our modeling effort. But again, in reality, these are taxon-specific parameters (Sarhou et al. 2005; Maranon et al. 2013). More refined investigations of these taxonomic parameters in target systems will improve Chl *a* predictions.

In regard to DO, spring time concentrations were relatively unresponsive to changes in parameter values. Differently, summer months were sensitive to parameter changes, with influential parameters for DO being similar to those for Chl *a*. This overlap was caused by the relationship between DO and phytoplankton biomass and physiological state. Therefore, prediction of DO might be improved by increasing knowledge of the parameters mentioned above for improvement of Chl *a* prediction. Additionally, improvements may be made by increasing our knowledge of taxon-specific, physiological state-specific phytoplankton respiration coefficients (K_{resp}), which summer-time DO was sensitive to.

We anticipate that our model for SABS will be an ideal tool for resource managers who are interested in freshwater inflows and nutrient loadings to this system. More specifically, the model can be used to test future scenarios where inflows may be altered, which may involve a number of different scenarios, including the increase or decrease of daily or average inflows, or altered timing and magnitude of peak discharge events. Further, we envision a best-practice approach involving the use of multiple models where commonalities among them are analyzed, similar to what has been done before in the SABS (Turner et al. 2014). Such analyses may be used to pinpoint important ecosystem thresholds for inflows and nutrient loading that preserve ecosystem functioning, maintain food web interactions, and ultimately help protect higher trophic levels such as the blue crab and endangered whooping crane, which are found in the

SABS region. Our model also has the capability to be more than a regionally specific management tool. As described previously, it was developed using generalized ecological and physicochemical principles, making it transportable across estuarine ecosystems provided that the required model training is done for those systems.

Supplementary Information The online version contains supplementary material available at <https://doi.org/10.1007/s12237-023-01213-x>.

Funding This research was supported by a grant from the Texas Commission on Environmental Quality.

Data Availability The data that support the findings of this study are available from the corresponding author, SEC, upon reasonable request.

References

- Antonopoulos, V.Z., and S.K. Gianniou. 2003. Simulation of water temperature and dissolved oxygen distribution in Lake Vegoritis, Greece. *Ecological Modelling* 160 (1–2): 39–53.
- Arismendez, S.S., H.C. Kim, J. Brenner, and P.A. Montagna. 2009. Application of watershed analyses and ecosystem modeling to investigate land–water nutrient coupling processes in the Guadalupe Estuary, Texas. *Ecological Informatics* 4 (4): 243–253.
- Babin, M., D. Stramski, G. M. Ferrari, H. Claustre, A. Bricaud, G. Obolensky, and N. Hoepffner. (2003). Variations in the light absorption coefficients of phytoplankton, nonalgal particles, and dissolved organic matter in coastal waters around Europe. *Journal of Geophysical Research: Oceans* 108(C7).
- Barbier, E.B., S.D. Hacker, C. Kennedy, E.W. Koch, A.C. Stier, and B.R. Silliman. 2011. The value of estuarine and coastal ecosystem services. *Ecological Monographs* 81: 169–193.
- Brewin, R.J., X.A.G. Morán, D.E. Raitsos, J.A. Gittings, M.L. Calleja, M. Viegas, M.I. Ansari, N. Al-Otaibi, T.M. Huete-Stauffner, and I. Hoteit. 2019. Factors regulating the relationship between total and size-fractionated chlorophyll-a in coastal waters of the Red Sea. *Frontiers in Microbiology* 10: 1964.
- Brock, T.D. 1981. Calculating solar radiation for ecological studies. *Ecological Modelling* 14 (1–2): 1–19.
- Bruesewitz, D.A., W.S. Gardner, R.F. Mooney, L. Pollard, and E.J. Buskey. 2013. Estuarine ecosystem function response to flood and drought in a shallow, semiarid estuary: nitrogen cycling and ecosystem metabolism. *Limnology and Oceanography* 58: 2293–2309.
- Cagle, S.E., and D.L. Roelke. 2021. Relative roles of fundamental processes underpinning PEG dynamics in dimictic lakes as revealed by a self-organizing, multi-population plankton model. *Ecological Modelling* 462: 109793.
- Chen, X., S.E. Lohrenz, and D.A. Wiesenburg. 2000. Distribution and controlling mechanisms of primary production on the Louisiana-Texas continental shelf. *Journal of Marine Systems*. 25: 179–207.
- Cloern, J.E., C. Grenz, and L. Videgar-Lucas. 1995. An empirical model of the phytoplankton chlorophyll: Carbon ratio—the conversion factor between productivity and growth rate. *Limnology and Oceanography* 40 (7): 1313–1321.
- Costanza, R. 1997. Predictability, scale and biodiversity in coastal and estuarine ecosystems: implications for management. In *Frontiers in ecological economics*, 309–329. Edward Elgar Publishing.
- Day Jr, J.W., A. Yanez-Arancibia, W.M. Kemp, and B.C. Crump. 2013. Introduction to estuarine ecology. *Estuarine Ecology* 2.
- Dorado, S., T. Booe, J. Steichen, A.S. McInnes, R. Windham, A. Shepard, A.E.B. Lucchese, H. Preischel, J.L. Pinckney, S.E. Davis, D.L. Roelke, and A. Quigg. 2015. Towards an understanding of the interactions between freshwater inflows and phytoplankton communities in a subtropical estuary in the Gulf of Mexico. *PLoS One* 10: 1–23.
- Eppley, R.W. 1972. Temperature and phytoplankton growth in the sea. *Fishery Bulletin* 70 (4): 1063–1085.
- Gable, G.M. 2010. *Spatio-temporal patterns of biophysical parameters in a microtidal, bar-built, subtropical estuary of the Gulf of Mexico*. Texas A & M University. Doctoral dissertation.
- Gillanders, B.M., K.W. Able, J.A. Brown, D.B. Eggleston, and P.F. Sheridan. 2003. Evidence of connectivity between juvenile and adult habitats for mobile marine fauna: an important component of nurseries. *Marine Ecology Progress Series* 247: 281–295.
- Hansen, D.V., and M. Rattray Jr. 1966. New dimensions in estuary classification 1. *Limnology and Oceanography* 11: 319–326.
- Hildebrand, H.H., and G. Gunter. 1953. Correlation of rainfall with Texas catches of white shrimp, *Penaeus setiferus* (Linnaeus). *Transaction American Fisheries Society* 82: 151–155.
- Hitchcock, J.N., and S.M. Mitrovic. 2015. Highs and lows: the effect of differently sized freshwater inflows on estuarine carbon, nitrogen, phosphorus, bacteria and chlorophyll-a dynamics. *Estuarine, Coastal and Shelf Science* 156: 71–82.
- Hitchcock, J.N., S.M. Mitrovic, W.L. Hadwen, D.L. Roelke, I.O. Grouns, and A.M. Rohlf. 2016. Terrestrial dissolved organic carbon subsidizes estuarine zooplankton: an in-situ mesocosm study. *Limnology and Oceanography*. 61: 254–267.
- Hu, X., H. Yao, C.J. Staryk, M.R. McCutcheon, M.S. Wetz, and L. Walker. 2020. Disparate responses of carbonate system in two adjacent subtropical estuaries to the influence of Hurricane Harvey—a case study. *Frontiers in Marine Science* 7: 26.
- Huisman, J. 1999. Population dynamics of light-limited phytoplankton: microcosm experiments. *Ecology* 80: 202–210.
- Islam, M.S., J.S. Bonner, B.L. Edge, and C.A. Page. 2014. Hydrodynamic characterization of Corpus Christi Bay through modeling and observation. *Environmental Monitoring and Assessment* 186: 7863–7876.
- Kennish, M.J. 2002. Environmental threats and environmental future of estuaries. *Environmental Conservation* 29: 78–107.
- Ketchum, B.H. 1951. The flushing of tidal estuaries. *Sewage and Industrial Wastes* 23: 198–209.
- Ketchum, B.H. 1954. The relation between circulation and planktonic populations in estuaries. *Ecology* 35: 191–200.
- Ketchum, B. H. 1983. Estuarine characteristics. *Ecosystems of the World* 1983.
- Laing, I., and R.-M. Chang. 1998. Hatchery cultivation of Pacific oyster juveniles using algae produced in outdoor bloom-tanks. *Aquaculture International* 6: 303–315.
- Lehrter, J.C., and C. Le. 2017. Satellite derived water quality observations are related to river discharge and nitrogen loads in Pensacola Bay, Florida. *Frontiers in Marine Science* 4: 274. <https://doi.org/10.3389/fmars.2017.00274>.
- Letelier, R.M., R.R. Bidigare, D.V. Hebel, M. Ondrusek, C.D. Winn, and D.M. Karl. 1993. Temporal variability of phytoplankton community structure based on pigment analysis. *Limnology and Oceanography* 38: 1420–1437.
- Mandal, S., S. Ray, and P.B. Ghosh. 2012. Modeling nutrient (dissolved inorganic nitrogen) and plankton dynamics at Sagar island of Hooghly-Matla estuarine system, West Bengal, India. *Natural Resource Modeling* 25 (4): 629–652.
- MacIntyre, H.L., and R.J. Geider. 1996. Regulation of Rubisco activity and its potential effect on photosynthesis during mixing in a turbid estuary. *Marine Ecology Progress Series* 144: 247–264.
- Maranon, E., P. Cermenon, D.C. Lopez-Sandoval, T. Rodriguez-Ramos, C. Sobrino, M. Huete-Ortega, J.M. Blanco, and J. Rodriguez.

2013. Unimodal size scaling of phytoplankton growth and the size dependence of nutrient uptake and use. *Ecology Letters* 16: 371–379.
- Michaud, J.P. 1991. A citizen's guide to understanding and monitoring lakes and streams. Publ., 94–149. Washington State Department of Ecology, Publications Office, Olympia, WA, USA 360–407–7472.
- Montagna, P., B. Vaughan, and G. Ward. 2011. The importance of freshwater inflows to Texas estuaries. *Water policy in Texas: responding to the rise of scarcity*, 107–127.
- Moore, M.L. 1989. *NALMS management guide for lakes and reservoirs*. North American Lake Management Society, P.O. Box 5443, Madison, WI, 53705–5443, USA.
- Mortimer, C.H. 1981. The oxygen content of air-saturated freshwaters over ranges of temperature and atmospheric pressure of limnological interest. *Mitteilungen Internationale Vereinigung Für Theoretische Und Angewandte Limnologie* 21: 1–23.
- Mullin, M.M., P.R. Sloan, and R.W. Eppley. 1966. Relationship between carbon content, cell volume, and area in phytoplankton. *Limnology and Oceanography* 11 (2): 307–311.
- Nordhaus, I., D.L. Roelke, R. Vaquer-Sunyer, and C. Winter. 2018. Coastal systems in transition from a 'natural' to an 'anthropogenically-modified' state. *Estuarine, Coastal and Shelf Science*. 211: 1–5.
- Odum, H.T. 1956. Primary production in flowing waters I. *Limnology and Oceanography* 1 (2): 102–117.
- Odum, W.E., E.P. Odum, and H.T. Odum. 1995. Nature's pulsing paradigm. *Estuaries* 18: 547–555.
- Olivieri, R., and F.P. Chavez. 2000. A model of plankton dynamics for the coastal upwelling system of Monterey Bay, California. *Deep-Sea Research II* 47: 1077–1106.
- Örnólfsson, E.B., S.E. Lumsden, and J.L. Pinckney. 2004. Nutrient pulsing as a regulator of phytoplankton abundance and community composition in Galveston Bay, Texas. *Journal of Experimental Marine Biology and Ecology* 303: 197–220.
- Palmer, T.A., and P.A. Montagna. 2015. Impacts of droughts and low flows on estuarine water quality and benthic fauna. *Hydrobiologia* 753 (1): 111–129.
- Paudel, B., and P.A. Montagna. 2014. Modeling inorganic nutrient distributions among hydrologic gradients using multivariate approaches. *Ecological Informatics* 24: 35–46.
- Pendleton, L.H. 2010. The economic and market value of coasts and estuaries: what's at stake? *The economic and market value of coasts and estuaries: what's at stake?*
- Pinckney, J.L., A. Quigg, and D.L. Roelke. 2017. Interannual and seasonal patterns of estuarine phytoplankton diversity in Galveston Bay, Texas, USA. *Estuaries and Coasts* 40: 310–316.
- Redfield, A. C. (1934). On the proportions of organic derivatives in sea water and their relation to the composition of plankton (Vol. 1). Liverpool: university press of liverpool.
- Robson, B.J., and D.P. Hamilton. 2003. Summer flow event induces a cyanobacterial bloom in a seasonal Western Australian estuary. *Marine and Freshwater Research* 54: 139–151.
- Roelke, D.I., L.A. Cifuentes, and P.M. Eldridge. 1997. Nutrient and phytoplankton dynamics in a sewage-impacted gulf coast estuary: a field test of the PEG-model and Equilibrium Resource Competition theory. *Estuaries* 20 (4): 725–742.
- Roelke, D.L. 2000. Copepod food-quality threshold as a mechanism influencing phytoplankton succession and accumulation of biomass, and secondary productivity: a modeling study with management implications. *Ecological Modelling* 134 (2–3): 245–274.
- Roelke, D.L., and R.H. Pierce. 2011. Effects of inflow on harmful algal blooms – some considerations. *Journal of Plankton Research* 33: 205–210.
- Roelke, D.L., H.-P. Li, N.J. Hayden, C.J. Miller, S.E. Davis, A. Quigg, and Y. Buyukates. 2013. Co-occurring and opposing freshwater inflow effects on phytoplankton biomass, productivity and community composition of Galveston Bay, USA. *Marine Ecology Progress Series* 477: 61–76.
- Roelke, D.L., H.-P. Li, C.J. Miller, G.M. Gable, and S.E. Davis. 2017. Regional shifts in phytoplankton succession and primary productivity in the San Antonio Bay System (USA) in response to diminished freshwater inflows. *Marine and Freshwater Research* 2017 (68): 131–145.
- Roelke, D.L., J. Bhattacharyya. 2017. Relationships between inflows, nutrient loading, phytoplankton and dissolved oxygen in two bay systems of the western Gulf of Mexico: a numerical modeling study (U.S. EPA Grant No. I9C8665308).
- Rose, K.C., P.J. Neale, M. Tzortziou, C.L. Gallegos, and T.E. Jordan. (2019). Patterns of spectral, spatial, and long-term variability in light attenuation in an optically complex sub-estuary. *Limnology and Oceanography* 64(S1): S257–S272.
- Roy, U., N.C. Majee, and S. Ray. 2016. Temperature dependent growth rate of phytoplankton and salinity induced grazing rate of zooplankton as determinants of realistic multi-delayed food chain model. *Modeling Earth Systems and Environment* 2 (3): 1–11.
- Russell, M.J., P.A. Montagna, and R.D. Kalke. 2006. The effect of freshwater inflow on net ecosystem metabolism in Lavaca Bay, Texas. *Estuarine, Coastal and Shelf Science* 68: 231–244.
- Sarthou, G., K.R. Timmermans, S. Blain, and P. Treguer. 2005. Growth physiology and fate of diatoms in the ocean: a review. *Journal of Plankton Research*. 53: 25–42.
- Shao, M., G. Zhao, S.C. Kao, L. Cuo, C. Rankin, and H. Gao. 2020. Quantifying the effects of urbanization on floods in a changing environment to promote water security—a case study of two adjacent basins in Texas. *Journal of Hydrology* 589: 125154.
- Slack, R.D., W.E. Grant, S.E. Davis III, T.M. Swannack, J. Wozniak, D.M. Greer, and A.G. Snelgrove. 2009. *Linking freshwater inflows and marsh community dynamics in San Antonio Bay to whooping cranes. San Antonio Guadalupe Estuarine System (SAGES)*, 188. Final Report.
- Spatharis, S., D.B. Danielidis, and G. Tsirtsis. 2007a. Recurrent Pseudo-nitzschia calliantha (Bacillariophyceae) and Alexandrium insuetum (Dinophyceae) winter blooms induced by agricultural runoff. *Harmful Algae* 6: 811–822.
- Spatharis, S., G. Tsirtsis, D.B. Danielidis, T.D. Chi, and D. Mouillot. 2007b. Effects of pulsed nutrient inputs on phytoplankton assemblage structure and blooms in an enclosed coastal area. *Estuarine, Coastal and Shelf Science* 73: 807–815.
- South Central Regional Water Planning Group, Region L. 2020. 2021 Regional Water Plan: Vol I.
- Thomann, R.V., and J.A. Mueller. 1987. *Principles of surface water quality modeling and control*. New York, USA: Harper and Row Publishing.
- Tolan, J.M. 2008. Larval fish assemblage response to freshwater inflows: a synthesis of five years of ichthyoplankton monitoring within Nueces Bay, Texas. *Bulletin of Marine Science* 82: 275–296.
- Turner, E.L., D.A. Bruesewitz, R.F. Mooney, P.A. Montagna, J.W. McClelland, A. Sadvoski, and E.J. Buskey. 2014. Comparing performance of five nutrient phytoplankton zooplankton (NPZ) models in coastal lagoons. *Ecological Modelling* 277: 13–26.
- Walker, L.M., P.A. Montagna, X. Hu, and M.S. Wetz. 2021. Timescales and magnitude of water quality change in three Texas estuaries induced by passage of Hurricane Harvey. *Estuaries and Coasts* 44: 960–971.
- Webster, I.T., and G.P. Harris. 2004. Anthropogenic impacts on the ecosystems of coastal lagoons: modelling fundamental biogeochemical processes and management implications. *Marine and Freshwater Research* 55: 67–78.
- Withrow, F.G. D.L. Roelke, R.M. Muhl, and J. Bhattacharyya. 2018. Water column processes differentially influence richness and diversity of neutral, lumpy and intransitive phytoplankton assemblages. *Ecological Modelling* 370: 22–32.

Wozniak, J.R., T.M. Swannack, R. Butzler, C. Llewellyn, and S.E. Davis III. 2012. River inflow, estuarine salinity, and Carolina wolfberry fruit abundance: linking abiotic drivers to Whooping Crane food. *Journal of Coastal Conservation* 16: 345–354.

Springer Nature or its licensor (e.g. a society or other partner) holds exclusive rights to this article under a publishing agreement with the author(s) or other rightsholder(s); author self-archiving of the accepted manuscript version of this article is solely governed by the terms of such publishing agreement and applicable law.